Stochastic methods for slip prediction in a sheared granular system

P. Bretz [1,*] L. Kondic,[2,†] and M. Kramar[1,‡]

[1]*Department of Mathematics, University of Oklahoma, Norman, Oklahoma 73019, USA*
[2]*Department of Mathematical Sciences, New Jersey Institute of Technology, Newark, New Jersey 07102, USA*

We consider a sheared granular system experiencing intermittent dynamics of stick-slip type via discrete element simulations. The considered setup consists of a two-dimensional system of soft frictional particles sandwiched between solid walls, one of which is exposed to a shearing force. The slip events are detected using stochastic state space models applied to various measures describing the system. The amplitudes of the events spread over more than four decades and present two distinctive peaks, one for the microslips and the other for the slips. We show that the measures describing the forces between the particles provide earlier detection of an upcoming slip event than the measures based solely on the wall movement. By comparing the detection times obtained from the considered measures, we observe that a typical slip event starts with a local change in the force network. However, some local changes do not spread globally over the force network. For the changes that become global, we find that their size strongly influences the further behavior of the system. If the size of a global change is large enough, then it triggers a slip event; if it is not, then a much weaker microslip follows. Quantification of the changes in the force network is made possible by formulating clear and precise measures describing their static and dynamic properties.

I. INTRODUCTION

Stick-slip dynamics is ubiquitous in granular and soft matter systems as well as in many other ones, see Refs. [1,2] for reviews. Understanding the intermittent stick-slip dynamics is of utmost importance because of the relevance to large-scale possibly cataclysmic events such as earthquakes. Therefore, there is a large body of research focusing on quantifying and explaining intermittency in a variety of systems, see Refs. [1,3–5] for reviews. For obvious reasons, there is an active interest in identifying precursors to the slip events that lead to abrupt structural rearrangements of the systems, see Refs. [6,7] for recent examples in the context of earthquakes. Extensive research considering acoustic precursors of intermittent dynamics in laboratory experiments can be found in Refs. [8,9] and references therein.

The attempts to identify precursors of slip events, fractures, and shear bands have a long history; for brevity here we discuss only recent developments. Several precursors are identified in various experimental systems [10–13]. These works report the existence of structural rearrangements of particles and point out that they become more prominent as a slip event approaches. Consistent results are also obtained in simulations [14–21]. However, despite a large amount of work concerned with identifying the precursors of slip events, we are not aware that they have been used for predictive purposes so far.

———————
*pbretz@ou.edu
†kondic@njit.edu
‡miro@ou.edu

In our recent work [22], we considered a two-dimensional (2D) system of soft disklike particles simultaneously exposed to compression and shear, see Fig. 1(a). If the pressure is sufficiently large and the shearing speed is sufficiently small, then this system is found to exhibit intermittent dynamics of the stick-slip type [16]. By analyzing the outcome of discrete element simulations (DEMs), in Ref. [22] we demonstrate a fundamental difference between the measures defined as system-wide averages, and the measures that quantify the evolution of the system on a micro (particle) or mesoscale scale. The system-wide averages are found to be almost insensitive to an approaching slip, while the latter measures show a promising potential to serve as precursors of slip events, and will be considered in the present paper.

One significant obstacle in using the measures quantifying the evolution of the system on a micro- or mesoscale for predicting an approaching slip event is that they are rather noisy and exhibit considerable variations between individual slip events. The method for delineating the slip events introduced in Ref. [22] is based on the wall velocity and requires the knowledge of the whole data set. Therefore, to identify the start of a slip event at time t_0, the data for both $t \leqslant t_0$ and $t > t_0$ are used. We will refer to this method as the off-line method and note that such an approach, while logical and commonly used, is not suitable for predictive purposes.

In the present paper, we develop a method that can predict the slip events on the fly for an incoming stream of data. We will refer to this method as the online method. The online method implemented in this paper is based on stochastic state space models (SSSMs) [23] that are often used to model an observable signal by decomposing it into several dynamic components, such as trend (steadily increasing or decreasing
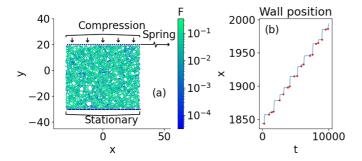
FIG. 1. (a) Snapshot of simulated particles at a fixed time, with the magnitude of the normal force on each particle shown on the logarithmic scale. The top and bottom walls are rigid rows of particles; the bottom wall is fixed and the top wall is exposed to normal ($-y$ direction) compression and to horizontal ($+x$ direction) elastic force. (b) The x position of the top wall for the first 10000 time outputs. The red dots mark the start of slip events determined by the off-line method described in II C 1.

part of the signal), seasonal (oscillations of the signal with different frequencies), or regressive components. Typically, these components are not directly observable but they can be modeled and used to predict the future values of the signal. SSSMs have been successfully used in meteorology [24], in robotics to guide autonomous vehicles [25] and track submarines [26], as well as in economics [27,28]. A closely related application to our problem can be found in Ref. [29] where the authors consider stochastic methods for modeling high-dimensional nonstationary spatiotemporal data collected at the sites with geological hazards. Another related application is the usage of machine learning to identify spatiotemporal clusters of surface displacement that are indicative of an imminent rock slide [30].

The applicability of SSSMs stems from the fact that the behavior of the considered measures is fundamentally different during the stick and slip regimes. The SSSMs allow us to predict the next value of a considered measure with good accuracy as long as the system is in the stick regime. The model is designed in such a way that it is too rigid to adapt to the evolution of the measure during the slip regime and its predictions become inaccurate when the system enters this regime. Thus, to detect the start of a slip event, we analyze the differences between the values predicted by the SSSM, and the observed values. In particular, we identify the start of a slip event as the time at which the error in our predictions becomes larger than a maximal acceptable value of the error, T_e. As we will see, the online method based on SSSMs is rather general and can be in principle applied to any scalar measure that describes the evolution. Naturally, the upcoming slip event can be detected in advance only if the behavior of the considered measure changes before the slip event starts. For this reason, it is important to identify appropriate measures to consider. Here, we are guided by our previous work [22], which shows the predictive potential of the measures based on force networks. We will show in particular that the measures that are sensitive to local changes in the force network provide appropriate input to SSSMs.

One important part of the present paper is the investigation of how the detection time of the slip events depends on the

considered measure and the value of T_e. As the value of T_e decreases, the upcoming slip events are detected earlier but the number of false positives increases. We will see that these false positives correspond to the so-called microslips, which were reported in previous work on granular systems, see, e.g., Refs. [16,31–34], or local changes of the force network and possibly particle positions that do not lead to wall motion, see also Ref. [21]. By using SSSMs, we find that there is a clear separation between the slip events and microslips, similarly observed in previous works [34,35].

We also show that both slip events and microslip events are initiated by a local change of the force network, which first becomes global by spreading over the network, and only afterward does the shearing wall start moving. Some local changes dissipate instead of spreading and therefore do not lead to slip or microslip events. This connection between local and global changes and resulting wall activity has been discussed in the literature, see, e.g., Refs. [15,21,36,37]; however, the advancement in quantification of force networks and data analysis implemented in the present work now allows that connection to be explored for predictive purposes.

The rest of this paper is organized as follows. Section II A describes the simulated system, and the measures used for predictions are presented in Sec. II B. In Sec. II C we introduce the framework for model-based slip detection. The general framework for stochastic models and the Kalman filter are reviewed in Sec II C 2, while the models for the considered measures are specified in Sec. II C 3. The main results are presented in Sec. III, followed by the conclusions in Sec. IV.

II. METHODS

A. Discrete element simulations

The simulations of dense granular material are carried out within a setup that leads to the stick-slip dynamics [22]. The simulation techniques are identical to the ones described in detail in the previous work [38] and here we provide just a summary. The material parameters used are motivated by experiments with photoelastic particles described, e.g., in Ref. [39]. Figure 1 illustrates the simulated system and its behavior. The granular particles are modeled as two-dimensional soft frictional disks. We place 2500 disks (system particles) between two horizontal rough walls placed parallel to the x axis, see Fig. 1(a). The system particles are bidisperse, with 25% of large particles and 75% of small particles with a size ratio of 1.25:1. The walls are constructed from small particles, which are at a fixed distance from each other, see Ref. [22]. The bottom wall is kept fixed, while the top one is pulled by a harmonic spring moving with the velocity v_{spring} in the $+x$ direction.

The linear spring-dashpot model is used to describe the interactions between the system particles and between the system and wall particles. We use the diameter of small particles, d, as the length scale, their mass, m, as the mass scale, and the binary collision time, τ_c, as the time scale. Motivated by experiments [39], we use $d = 1.27$ cm, $m = 1.32$ g, and $\tau_c = 1.25 \times 10^{-3}$ s, as appropriate for particles of Young modulus of $Y \approx 0.7$ MPa. Then, the normal spring constant is $k_n = m\pi^2/2\tau_c^2 \approx 4.17$ N/m, and the tangential spring constant

(needed for modeling of tangential forces using the Cundall-Strack model [40]) is taken as $k_t = 6k_n/7$. The coefficient of static friction, μ, is equal to 0.7 for particle-particle contacts and $\mu = 2$ for particle-wall contacts (using a larger value here to reduce slipping of the system particles relative to the walls). The force constant of the spring applied to the top wall, k_s, is significantly smaller than the one describing particle interactions, $k_s = k_n/400$. The (constant) restitution coefficient is 0.5. In addition, a normal compression force is applied in the $-y$ direction to model an externally applied pressure (force or length in two dimensions) of $p = 0.02$; gravitational effects are not included. We note that with our choice of units, the numerical value of the applied pressure is of the same order of magnitude as the average overlap (compression) of the particles.

Stick-slip dynamics occurs for sufficiently large applied pressure and for sufficiently slow shearing, see, e.g. Ref. [16]. For $p = 0.02$ we find by experimenting that the value $v_{\text{spring}} = 1.5 \times 10^{-3}$ leads to stick-slip dynamics. Then, we integrate Newton's equations of motion for both the translation and rotational degrees of freedom using a fourth-order predictor-corrector method with time step $dt = 0.02$. The states of the system, used to compute the quantities presented in this paper, are stored at times $\delta t = 10dt$ apart. In this paper, all the figures that show time-dependent results are in units of δt.

The simulations start by applying a pressure p to the top wall and then letting the system relax until the ratio of kinetic or potential energy becomes sufficiently small [22]. Then we start moving the spring in the $+x$ direction, and, after the initial transient regime disappears, start collecting data. Figure 1(b) shows the horizontal position of the top wall for a short time window; the red dots illustrate the starts of slip events obtained using the off-line method summarized in Sec. II C 1. The complete simulation contains 5×10^5 time output [first 10^4 outputs are shown in Fig. 1(b)] and hundreds of slip events.

B. Measures

The analysis and detection of the slip events are based on three different measures whose potential was identified in Ref. [22]. The first one, shown in Fig. 2(a), is the horizontal velocity, $v_x(t)$, of the top wall. The next measure is based on the properties of the differential force network; to define this network, we first discuss the concepts of the contact and force networks. The contact network, CN(t), is a graph with one vertex at the center of each particle (excluding those in the top and bottom walls). There is an edge between two vertices of CN(t) if the particles corresponding to these vertices are in contact at time t. The force network FN(t) is obtained by assigning weights to the edges in CN(t), representing the magnitudes of the normal force acting between the corresponding particles. A differential force network, DFN(t), represents the differences between the force networks computed at two consecutive samples at t and $t + \delta t$. Its edges are given by the union of the edges in the weighted graphs FN(t) and FN$(t + \delta t)$. The weight on an edge in DFN(t) is the absolute value of the difference of the weights assigned to this edge in FN$(t + \delta t)$ and FN(t) if the edge is present in both. If the edge is not present in one of the force networks,
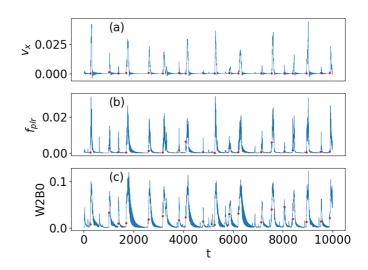

FIG. 2. Sample of the evolution for the first 10000 outputs: (a) the magnitude of the velocity, v_x, of the top wall, (b) the left-right percolation force, f_{plr}, and (c) the Wasserstein distance, W2B0. All the quantities are defined in Sec. II B. The red dots mark the start of slip events determined by the off-line method described in Sec. II C 1. Here, v_x shows two alternating regimes of behavior: long periods of stick regime, in which the wall moves slowly or not at all, and shorter periods of slip and microslip events, when the wall moves rapidly. The time axis is in units of δt, as specified in Sec. II A.

we consider the corresponding weight in that force network to be zero. Figure 3 depicts typical force and differential force networks during a stick regime and at the onset of a slip event.

The measure that we use in what follows is the maximal force, $f_{plr}(t)$, for which DFN(t) percolates between the left and right boundary of the domain (in Ref. [22] top-bottom percolation was considered as well, but we do not use that measure here for brevity).
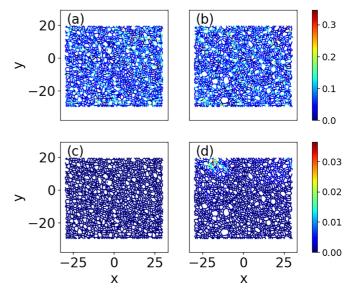

FIG. 3. Examples of the force network FN(t) (a)–(b) and differential force network DFN(t) (c)–(d) where (a), (c) depict a time well before a slip event and (b), (d) depict a time at the onset of a slip event. Note that relatively high values of differential force are present at the onset of the slip event.

The last measure quantifies the time evolution of the force network. For each force network, FN(t), we compute its persistence diagrams PD$_0(t)$ defined briefly here, and more fully in Ref. [41]; persistence diagrams were extensively used in our earlier works in the analysis of granular matter in various settings, see, e.g., Refs. [42–44]. PD$_0(t)$ describes the structure of the superlevel sets of the force network FN(t). In particular, PD$_0(t)$ is a finite collection of points in (b, d) such that $b > d$. Every point (b, d) in PD$_0(t)$ indicates that a connected component appears in the set consisting of the edges of FN(t) with weights larger than b and it merges with another connected component after adding all the edges with the weights larger than d. To help interpretation, we note that the points in PD$_0(t)$ with b coordinate sufficiently large (larger than the average force) describe the vague concept of force chains. In the present work, for simplicity, we do not consider loops that could be described similarly by a separate PD$_1(t)$, see Ref. [22] for more details.

The difference between two persistence diagrams can be measured by their Wasserstein distance defined precisely in Ref. [42]. This distance essentially sums up all the changes between the persistence diagrams in a manner analogous to the L_2 norm. In what follows, we encode the changes between the force networks FN(t) and FN$(t + \delta t)$ by considering the Wasserstein distance, W2B0(t) between their PD$_0$ persistence diagrams.

Figure 2 illustrates the measures described above. At the start of the slip events detected by the off-line method, described in Sec. II C 1, the value $v_x(t)$ is still relatively close to its baseline typical for the stick regime. This is not the case for the other two measures. In particular, W2B0(t) increases considerably before the detection time. We exploit this behavior to develop an online method for detecting slip events that can produce an early warning before $v_x(t)$ increases significantly.

C. Methods for detecting slip events

Figure 4 shows the stick-slip dynamics in more detail, with three illustrative examples of the behavior of the time series, v_x (since there is no possibility of confusion, we drop the time dependence from now on). Even though the peaks of v_x are well pronounced during the slip events, it is nontrivial to precisely define when individual events start. Difficulties in defining the start of a slip event arise from the oscillations of v_x, visible in Fig. 4. In the considered system these oscillations are related to propagating elastic waves caused by the vertical (y) component of motion of the top wall, which is associated with each slip event [22].

Due to these complications, slip detection must be done carefully. One option is to employ an off-line method that uses the values of v_x after the slip event has begun to distinguish it from oscillations; this approach was used in Ref. [22] and is outlined in Sec. II C 1. Related methods were used in other works facing similar issues, see, e.g., Refs. [21,34]. An alternative is to use a more sophisticated online method that accounts for the oscillations. Stochastic state space models (SSSMs), discussed later in this section, provide a good framework for such an approach. To present the main idea, we use an example of v_x. Note that the amplitude of the oscillations of v_x can vary and tends to decrease as we
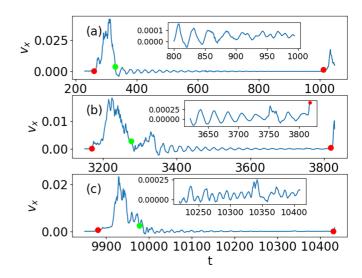

FIG. 4. Examples of three slip events showing the magnitude of the wall velocity, v_x. The red (green) dots mark the start (end) of the slip event detected by the off-line method presented in Sec. II C 1. Note that during the stick regime, v_x oscillates with decreasing amplitude around a roughly constant value. The insets zoom into the time just before the following slip event.

approach the onset of a slip event. Therefore, v_x during a stick can be modeled as a composition of several components. One component represents the level around which the oscillations occur, and several harmonic components with stochastically changing amplitudes reasonably reproduce the oscillations. To detect the start of a slip event based on v_x, we exploit the fact that the behavior of this quantity is fundamentally different during the stick and slip regimes. So, the SSSM used to model the evolution during the stick regime does not provide good predictions if the system is not in this regime. This means that during slip events, the difference between the value predicted by the SSSM and the observed one becomes large. Thus, to identify the start of slip events we just need to detect when the difference between the predictions and observed values becomes sufficiently large.

Section III demonstrates that SSSMs can be used to devise an efficient online method for detecting the start of slip events. In particular, we will see that the algorithm tends to detect upcoming slip events earlier than the off-line approach. This result opens the door for a real-time prediction of slip events. In what follows, we first review the off-line approach in Sec. II C 1, followed by a short background of stochastic models and Kalman filter in Sec. II C 2.

1. Off-line approach for detecting slip events

In the rest of this paper we will call slip events the events that are detected by this approach. To deal with the oscillations present in v_x, shown in Fig. 4, the off-line approach for detecting slip events [22] relies on a choice of two thresholds. The value of the first threshold, $v_l = 2 \times 10^{-3}$, is larger than the amplitude of the oscillations visible in the examples shown in Fig. 4, so the method avoids spurious detection of slip events. If v_x exceeds v_l, then a slip event is identified at time t. However, at this time the wall has already begun to move with a non-negligible speed. For this reason, the off-line method
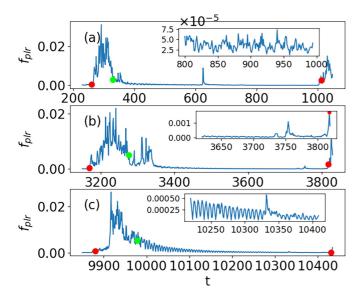
FIG. 5. The percolation measure, f_{plr}, for the same time samples shown in Fig. 4; the meaning of the red and green dots is as discussed in the caption of Fig. 4.

FIG. 6. The W2B0 measure for the same time samples in Fig. 4. Note the events at $t = 650$ in (a), $t = 3750$ in (b), and $t = 10350$ in (c); these are examples of internal, local changes of the W2B0 measure that do not result in a slip event. The meaning of the red and green dots is as discussed in the caption of Fig. 4.

uses a second smaller threshold, $v_s = 2.5 \times 10^{-4}$, to find more precisely the start of each slip event. For this purpose, the algorithm moves back in time until the value of v_x drops below v_s. The time when this occurs is the starting point of the slip (the numerical values used for v_l and v_s are motivated in Ref. [22]). The end of a slip event is identified as the time at which v_x as well as its average over the next 50 outputs (roughly two periods of oscillations following a slip event) is smaller than v_l. This algorithm is slightly different than the one detailed in Ref. [22], which uses the condition that the average over the preceding 50 outputs marks the end of a slip event. We make this change to avoid artificial termination of a slip event, which occurs when v_x drops briefly below v_l at the start of a slip event.

The main shortcoming of this approach (or any other approach based on using both past and future data for slip detection), is that it cannot be used for real-time detection of slip events. It detects the time at which the event starts only after the wall velocity exceeds the specified threshold. Moreover, the precise values of the thresholds influence the number and length of the detected events.

2. State space models and Kalman filter

As discussed at the beginning of Sec. II C, during the stick regime the signal specified by v_x can be approximated by a composition of several components, one of them representing the level around which oscillations occur, and the rest describing oscillations. The behavior of the other measures is more complex. Figures 5 and 6 show the f_{plr} and W2B0 measures during the same time windows as in Fig. 4. For example, to model W2B0, we have to account for both the oscillations and a decreasing trend of the signal.

We proceed by presenting the general idea behind stochastic modeling of a time series y_t, which can be decomposed into several components whose characteristics are captured by the value of the state vector $\boldsymbol{\theta}$, which encodes the properties
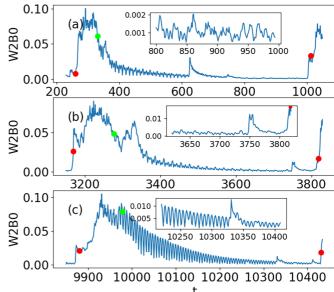
such as trend and oscillations of a considered measure. As commonly done in the literature [23], we use a discrete time $t \in \mathbb{N}$ for the rest of this section, where t is in units of δt, specified in Sec. II A. For example, if y_t represents the magnitude of the wall velocity, v_x, then $y_t = v_x(t)$, the wall velocity at the physical time $t * \delta t$. To model the time series y_t by a sequence of random variables Y_t we will use a special class of SSSMs known as dynamical linear models (DLMs). This choice is motivated by two independent factors. First, the necessary computations can be performed efficiently. Second, the models are sufficiently rich to properly capture the evolution of the considered measures during the stick regime while they are too rigid to assimilate the time evolution of these measures during the slip regime.

The main assumption of the DLMs is that the evolution of the n-dimensional state vector, $\boldsymbol{\theta}_t$, is governed by a real Markov chain called the state process and the random variable Y_t is a noisy (imprecise) scalar observation of this chain. To be more precise, the evolution of $\boldsymbol{\theta}_t$ is described by the equation

$$\boldsymbol{\theta}_t = G_t \boldsymbol{\theta}_{t-1} + \boldsymbol{w}_t \tag{1}$$

while the values Y_t can be reconstructed from $\boldsymbol{\theta}_t$ via the equation

$$Y_t = F_t \boldsymbol{\theta}_t + v_t, \tag{2}$$

where $(G_t)_{t \geqslant 1}$ and $(F_t)_{t \geqslant 1}$ are known sequences of matrices of order $n \times n$ and $1 \times n$, respectively. Two independent sequences of random variables describing the observation error, $(v_t)_{t \geqslant 1}$, and the model error, $(\boldsymbol{w})_{t \geqslant 1}$, are distributed according to zero mean normal distributions $v_t \sim \mathcal{N}_1(0, V_t)$ and $\boldsymbol{w}_t \sim \mathcal{N}_n(\mathbf{0}, W_t)$, where the variances V_t and covariance matrices W_t are given. We will explain in Sec. II C 3 how to specify $G_t, F_t, W_t,$ and V_t for the measures considered in this paper.

Here we just note that the G_t models the evolution of the individual components of the signal and F_t describes how to combine these components to obtain the random variable Y_t, which models the time series y_t. The error (noise) terms are important because there might be external noise in the physical system and the relations described by G_t are only approximate.

Unlike in deterministic systems, the value of $\boldsymbol{\theta}_t$ is not known precisely. Instead, the probability that $\boldsymbol{\theta}_t$ has a given value is expressed by a probability distribution $\pi(\boldsymbol{\theta}_t)$, which in the case of DLMs is required to be a multivariate normal distribution. Given a DLM and the distribution $\pi(\boldsymbol{\theta}_{t-1})$, we can predict the value of $\boldsymbol{\theta}_t$ as

$$\hat{\boldsymbol{\theta}}_t = G_t \bar{\boldsymbol{\theta}}_{t-1}, \tag{3}$$

where $\bar{\boldsymbol{\theta}}_{t-1}$ is the mean value of $\pi(\boldsymbol{\theta}_{t-1})$. The predicted value, $\hat{\boldsymbol{\theta}}_t$, is known as the forecast and can be used to construct a prediction

$$\hat{Y}_t = F_t \hat{\boldsymbol{\theta}}_t \tag{4}$$

of the next value y_t of the modeled time series. In particular, if we know $\pi(\boldsymbol{\theta}_0)$, then Eqs. (3) and (4) allow us to predict the value of y_1. However, we usually do not know the initial distribution $\pi(\boldsymbol{\theta}_0)$. The fact that $\pi(\boldsymbol{\theta}_0)$ is not known can be overcome by using the iterative procedure known as the Kalman filter [23], which uses the Bayesian probability to improve our knowledge about the distribution of $\boldsymbol{\theta}_t$ by incorporating the observed data $y_0, \ldots y_t$. This is done by computing the conditional distribution $\pi(\boldsymbol{\theta}_t | Y_1 = y_1, \ldots, Y_t = y_t)$. In practice, if the DLM is an appropriate model for the time series y_t and the initial (prior) distribution $\pi(\boldsymbol{\theta}_0)$ is given by a normal distribution with large variance, then after a short burn-in period the conditional distribution $\pi(\boldsymbol{\theta}_t | Y_1 = y_1, \ldots, Y_t = y_t)$ describes the state $\boldsymbol{\theta}_t$ with reasonable accuracy, and the model provides satisfactory predictions of the future states of the time series y_t.

The precise definitions of G_t and F_t depend on the particular measure considered and will be provided in Sec. II C 3. On the other hand, to quantify the observation error and model error we use standard universal methods. Here we only provide their brief summary; detailed exposition is available [23]. The shape of the covariance matrix W_t for the model error is given by the discount factor method, i.e.,

$$W_t = \frac{1 - \delta}{\delta} P_t, \tag{5}$$

where P_t is the conditional covariance of $\pi(G_t \boldsymbol{\theta}_{t-1} | Y_1 = y_1, \ldots, Y_{t-1} = y_{t-1})$ and $\delta \in (0, 1]$ is the discount factor, which will be specified for the individual measures in Sec. II C 3. The value of δ corresponds to the overall accuracy with which G_t describes the state update from $t - 1$ to t, referred to in Ref. [23] as model trust. Note that if $\delta = 1$, then Eq. (3) does not contain noise, and the evolution of $\boldsymbol{\theta}_t$ is deterministic.

The variance V_t of the observation error is modeled by a time-invariant unknown random variable, σ^2, estimated from the data at each time t. To be compatible with the iterative scheme defined by the Kalman filter, the variable σ^2 has to be inverse gamma distributed. For the initial (prior) distribution $\pi(\sigma^2)$ we choose the inverse gamma distribution IG(2, 10^{-3}).

This is a vague prior in the Bayesian terminology; it expresses a high degree of uncertainty as to the value of the unknown σ^2. By choosing a vague prior, the distribution of σ^2 quickly responds to the data.

3. Specification of dynamical linear models (DLMs)

In this section we provide DLMs that model the evolution of the measures, defined in Sec. II B, during the stick regime. To specify a DLM for a given measure we start by specifying the components of the state vector $\boldsymbol{\theta}$ that capture the trend and oscillations of the signal. To describe the time evolution of the individual components of $\boldsymbol{\theta}$, given by the state process, Eq. (1), we need to set G_t and the covariance matrix W_t of the model error $\boldsymbol{w}_t$. We recall that W_t is specified by choosing the discount factor δ. Finally, to forecast the value of the modeled measure, by using Eq. (2), we need to specify the observation function, F_t, and the distribution of the observation error. As explained in Sec. II C 2, the observation error is modeled by a time-invariant random variable estimated from the data at each time t. The required initial distribution is always chosen to be the inverse gamma distribution $\pi(\sigma^2) \sim$ IG(2, 10^{-3}).

Figures 4–6 manifest that all considered measures exhibit oscillations, albeit with different frequencies. To model the oscillations we use a few harmonic components. For a given measure the frequency of the first harmonic component is set to its dominant frequency ω, determined by Fourier analysis of the first 10% of the signal. The frequencies of the other harmonic components are natural multiples of ω. So, for each model, we specify the number of harmonic components and the discount factor δ.

Our extensive numerical investigation shows that all results discussed in Sec. III are robust under rather large variations of the number of harmonic components and δ. The dominant frequency, ω, is more sensitive and needs to be estimated with the absolute error smaller than 0.01. The final choice of the parameters for each model was guided by diagnostics of the normalized prediction error (NME) of the model defined as

$$e_t = \frac{y_t - \hat{Y}_t}{\sqrt{Q_t}}, \tag{6}$$

where $Q_t = F_t(P_t + W_t)F_t' + V_t$, F_t' is the transpose of the matrix F_t and P_t is the conditional covariance of $\pi(G_t \boldsymbol{\theta}_{t-1} | Y_1 = y_1, \ldots, Y_{t-1} = y_{t-1})$. In other words, Q_t is a covariance of the conditional distribution of $\pi(Y_t | Y_1 = y_1, \ldots, Y_{t-1} = y_{t-1})$. If the model is a good fit for the data, then the NMEs are uncorrelated and they are distributed according to the standard normal distribution [23]. We use the Ljung-Box statistic to test [45] for possible autocorrelation and the Shapiro-Wilk test [46] to see if the normalized errors are distributed according to the standard normal distribution. We chose the models that yield the best diagnostics during the stick regimes shown in Figs. 4–6.

We start by setting up the model for the wall velocity, v_x. Figure 4 shows that during the stick regime v_x oscillates around an almost constant value. Note that oscillations exhibit multiple frequencies. Their dominant frequency $\omega = 0.25$ was determined from the first 10% of the data. These oscillations can be modeled satisfactorily with only two harmonic components with frequencies $\omega_i = i * \omega$, for $i = 1, 2$. The harmonic

component with the frequency ω_i is represented by a pair of two variables θ^{2i-1}, θ^{2i} that evolve in such a way that the point $(\theta_t^{2i-1}, \theta_t^{2i})$ rotates around a circle with the constant frequency ω_i. Without the error (noise) terms, the radius of this circle would be constant as well. However, the error terms allow for a slow change of this radius.

The value around which the oscillations occur is represented by the last component θ^5 of the state vector $\boldsymbol{\theta}$. The value of θ_t^5 changes very slowly, and on the deterministic level we consider θ_t^5 to be constant. We allow it to change only via the error term. The following equations, defining G_t, formalize the described evolution of the components of $\boldsymbol{\theta}$

$$\theta_t^{2i-1} = \theta_{t-1}^{2i} \sin \omega_i + \theta_{t-1}^{2i-1} \cos \omega_i, \tag{7a}$$

$$\theta_t^{2i} = \theta_{t-1}^{2i} \cos \omega_i - \theta_{t-1}^{2i-1} \sin \omega_i, \tag{7b}$$

$$\theta_t^5 = \theta_{t-1}^5, \tag{7c}$$

for $i = 1, 2$. We note that both variables $(\theta_t^{2i-1}, \theta_t^{2i})$, for each value $i = 1, 2$, oscillate with the same frequency and amplitude. Only their phase is different. To reconstruct the oscillations around the slowly changing value θ_t^5, it is sufficient to consider the variables θ_t^{2i-1} for $i = 1, 2$. The observation function, F_t, just adds the individual components of the signal and is defined as

$$F_t(\boldsymbol{\theta}_t) = \theta_t^1 + \theta_t^3 + \theta_t^5. \tag{8}$$

To specify the model error, $\boldsymbol{w}_t$, we use the discount factor $\delta = 0.6$. To initialize the DLM we need to define the initial (prior) distribution for the state $\boldsymbol{\theta}_0$. We use a normal distribution centered at mean $\bar{\boldsymbol{\theta}}_0$ where $\bar{\theta}_0^j = 0$, for $j = 1, \ldots 4$, $\bar{\theta}_0^5 = v_x(0)$, with the width specified by the scaled covariance matrix $\bar{C}_0 = I$.

Now we turn our attention to the left-right percolation force, f_{plr}, shown in Fig. 5. The dominant frequency of oscillations for this measure is $\omega = 0.54$. Again it is sufficient to use two harmonic components with frequencies $\omega_i = i * \omega$, $i = 1, 2$. As in the case of v_x, the evolution of the variables $\theta^1, \ldots, \theta^4$, representing the harmonic components, is described by Eqs. (7a) and (7b).

The most important difference between the behavior of v_x and f_{plr} is that the value around which f_{plr} oscillates is not changing slowly. This value decreases in an approximately linear manner. To incorporate this decrease into the model, we need two state components: θ_t^5, which models the slowly changing slope, and θ_t^6, which captures the decreasing value around which the signal oscillates. These two components evolve according to the following equations:

$$\theta_t^5 = \theta_{t-1}^5, \tag{9a}$$

$$\theta_t^6 = \theta_{t-1}^6 + \theta_{t-1}^5. \tag{9b}$$

The observation function, F_t, again sums the variables capturing the oscillations and the variable θ_t^6 representing the value around which the oscillations occur, so $F_t(\boldsymbol{\theta}_t) = \theta_t^1 + \theta_t^3 + \theta_t^6$. To specify the observation error we use the discount factor $\delta = 0.93$. As in the case of v_x, the initial distribution for the state vector $\boldsymbol{\theta}_0$ is a normal distribution centered at $\bar{\boldsymbol{\theta}}_0$ where $\bar{\theta}_0^j = 0$, for $j = 1, \ldots 5$, $\bar{\theta}_0^6 = f_{plr}(0)$ and the scaled covariance matrix $\bar{C}_0 = I$.

The last considered measure, W2B0, exhibits oscillations with the dominant frequency $\omega = 0.54$, and using two harmonic components is once again sufficient. The most important difference between the behavior of f_{plr} and W2B0 is that the value around which W2B0 oscillates decays in a roughly exponential manner, see Fig. 6. Thus, it can be modeled by a function $e^{\mu t}$ where the value of $\mu \leqslant 0$ is allowed to change slowly through the error term. To incorporate this exponential decrease in the model, we use two state components: θ_t^5, which models the slowly changing value μ, and θ_t^6, which captures the behavior of $e^{\mu t}$. The following equations ensure the desired evolution of these components:

$$\theta_t^5 = \theta_{t-1}^5, \tag{10a}$$

$$\theta_t^6 = \theta_{t-1}^6 e^{\theta_{t-1}^5}. \tag{10b}$$

The discount factor is $\delta = 0.67$ and the initial distribution for the state vector $\boldsymbol{\theta}_0$ is a normal distribution centered at $\bar{\boldsymbol{\theta}}_0$ where $\bar{\theta}_0^j = 0$, for $j = 1, \ldots 5$, $\bar{\theta}_0^6 = \text{W2B0}(0)$ and the scaled covariance matrix $\bar{C}_0 = I$.

Equation (10b) is nonlinear, so the model is not a DLM and the Kalman filter cannot be used to compute the necessary conditional distributions. To accommodate the nonlinearity of the function G_t, we use the extended Kalman filter (EKF) [24], which uses the Jacobian matrix of $G_t(\boldsymbol{m}_{t-1})$ to compute the covariance of the predictive distribution of $\boldsymbol{\theta}_t$. There are well-known divergence problems with EKF [24], since using the Jacobian matrix can lead to unrealistically small values of the covariance matrix of the state distribution. This can impede the ability of the filter to assimilate the observed data and eventually cause divergence of the model. In our case, this happens when the value of θ_t^6 becomes too small and is rounded to zero. To retain numerical integrity during our computations, we reinitialize the filter upon encountering filter divergence. We note that this occurred only once in the entire data set.

III. RESULTS

Now we are ready to show how the dynamical linear models (DLMs) defined in Sec. II C 3 can be used for the online detection of the slip events identified by the off-line method. We will see that the DLMs detect not only the slip events but also additional events. The DLMs based on the wall velocity, v_x, and the measure of the global change in the force network, f_{plr}, detect roughly the same events. However, the global changes of the force network are typically detected before the increased activity of the wall. The DLM based on W2B0, measuring local changes of the force network, identifies almost all events detected by the other two DLMs, and in addition, it detects extra events in which a local change of the force network appears but does not spread across the whole system. As expected, in events detected by both W2B0 and f_{plr}, the local changes of the force network are detected before the global changes.

A. Event detection by DLMs

By construction, the accuracy of the predicted values of a measure modeled by the DLM significantly deteriorates during the slip events detected by the off-line method. To
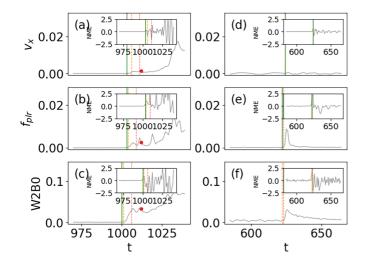
FIG. 7. Two detection examples: (a)–(c) a slip event detected by the off-line method [shown in Figs. 4(b), 5(b), and 6(b)], and (d)–(f) a microslip event. The measure v_x is shown in (a), (d), f_{plr} in (b), (e), and W2B0 in (c), (f). In (a)–(c), the red dots identify the start of the slip event determined by the off-line method. The insets show the respective NME for individual DLMs, with the vertical lines marking detection times for individual DLMs using three different values of $T_e = 0.1$, 0.4, and 1.5 for the solid green line, dashed orange line, and dotted red line, respectively.

FIG. 8. Probability density of (a) maximum of wall velocity v_x and (b) d_x, the wall displacement in the x direction, on the $\log_{10}$ scale during the events detected from the wall velocity. The bimodal nature of these distributions indicates presence of two classes commonly refereed to as slip and microslip events.

identify the events, during which the time evolution of a considered measure does not conform to the respective DLM, we choose a maximal acceptable value of the NME, T_e. The events detectable by the DLM and a given error threshold, T_e, are obtained as follows. The start of an event is considered to occur at time t_0 if the NME, e_t, satisfies $|e_{t_0-1}| < T_e$ and $|e_{t_0}| \geqslant T_e$. While one could define that the event ends when the value of $|e_t|$ drops below T_e, it is possible that the value of $|e_t|$ becomes accidentally small during a slip event detected by the off-line method. Therefore, to declare that the event ends at t_1, we require that all the values $|e_{t_1}|, |e_{t_1-1}|, \ldots, |e_{t_1-m}|$ are smaller than T_e. The value of m is chosen to be roughly one period of the dominant oscillations present during the stick regime (see, e.g., Fig. 4) corresponding to $m = 25$.

To illustrate the dependence of the starting time of a detected event on the value of T_e, we proceed by considering an example of two events detectable by all DLMs. The first event, shown in Figs. 7(a)–7(c), is a slip event detected by the off-line method. In contrast, Figs. 7(d)–7(f) show a microslip, which is not detected by the off-line method. This nomenclature is motivated by the literature [16,31–34], which also distinguishes slips and microslips. In the present work, microslips are defined as events that are not detected by the off-line method but are detected by the DLM based on v_x for $T_e = 0.1$. This particular value of T_e is motivated below. In what follows we will also see that there are events detectable only by the DLM based on W2B0. Any event detected by W2B0 for $T_e = 0.4$ which cannot be detected by the DLM for f_{plr} is called a local change; this particular numerical value is motivated below.

Figures 7(a)–7(c) compare detection times of a slip event obtained by DLMs of v_x, f_{plr}, and W2B0, respectively, for three different values of T_e. Clearly, decreasing the value of
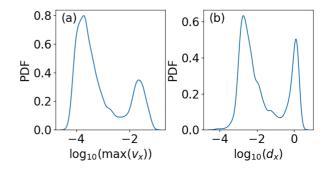
T_e leads to an earlier detection time. We note that for each fixed value of T_e, the DLM for W2B0 detects the event first, followed by f_{plr}, and then v_x.

Figures 7(d)–7(f) show a microslip event and illustrate some difficulties that may arise if a single threshold value, T_e, is chosen. Namely, the DLM for v_x does not detect this event for $T_e = 1.5$ and $T_e = 0.4$, since the NME rises only slightly above 0.1. On the other hand, using $T_e = 0.1$ for W2B0 does not lead to a transition detection inside the depicted time window. The start of the event is detected before the shown time window starts and the event lasts through the whole time window. Therefore, if T_e is too large, then slip events may be detected late or even missed, while choosing T_e too small may result in erroneously classifying parts of a stick regime as a slip, microslip, or local change event. For this reason, in what follows we will consider a range of T_e values.

Figure 8 motivates the above classification of the events into slips and microslips. It clearly shows that distributions of maximum velocity and magnitude of wall displacements, denoted by d_x, during the events detected by v_x are bimodal. We note that the slip and microslip events are roughly delineated by the valley separating the peaks.

With this example in mind, we now examine the entire data set. Figure 9(a) plots the number of events detected by DLMs for the considered measures. We observe that each of the measures shows a prominent peak, located at $T_e^c = 0.1$ for v_x and f_{plr}, and $T_e^c = 0.4$ for W2B0. If we decrease T_e below T_e^c (as specified for each of the measures), then distinct events start to merge and their number decreases. Eventually, as T_e approaches zero, all the events merge into a single one. Thus, from now on we will only consider the values of $T_e \geqslant T_e^c$. Note that earlier in this section, we used the value of $T_e^c = 0.1$ ($T_e^c = 0.4$) at which the largest number of events can be detected by v_x (W2B0) to define microslip (local change) events.

As the value of T_e increases, the number of detected events decreases. This is caused by the disappearance of events during which the NME does not exceed T_e, see, e.g., Fig. 7(d). Figure 9(a) shows that for v_x and f_{plr} there is a pronounced plateau followed by a gentle rise. Further investigation shows that some events are followed by almost immediate aftershocks, see Fig. 4(b). Detection of these aftershocks causes this rise because, for small values of T_e, the main event and
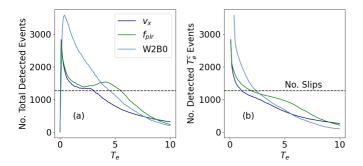
FIG. 9. (a) The total number of events detected by DLMs of v_x, f_{plr}, and W2B0 as a function of T_e. The curves corresponding to v_x and f_{plr} show a well-pronounced maximum at $T_e^c = 0.1$, while the curve corresponding to W2B0 shows a maximum at $T_e^c = 0.4$. The dashed line indicates the number of slip events detected by the off-line method. (b) The number of events after removing aftershocks, i.e., the number of events detected at T_e^c that are still detectable at T_e.

its aftershock are identified as one event; however, as T_e increases, both the main event and the aftershock are eventually identified as separate events. To avoid the identification of aftershocks as separate events and to accurately capture the number of distinct events, we consider an adjusted number of events, shown in Fig. 9(b). The aftershocks are removed by using the events detected at T_e^c as a baseline. Different events detected at $T_e \geqslant T_e^c$ are counted as one if they occur during a single event detected at T_e^c. The adjusted number of slip events decreases for all DLMs and values $T_e \geqslant T_e^c$.

B. Insight provided by different measures

We continue by investigating the relation between the events detected by DLMs for different measures at $T_e = T_e^c$. We say that two events detected by different measures are matched if the time intervals over which they take place overlap. By matching the events detected by v_x, we find that 93% of these events (slips and microslips) are also detected by f_{plr}. Moreover, 97% (98%) of the events detected by v_x (f_{plr}) are detected by W2B0. Hence, a disturbance of the wall, that causes the NME for v_x to exceed T_e^c, is typically accompanied by a local as well as global rearrangement of the force network detected by W2B0 and f_{plr}, respectively.

On the other hand, 28% (26%) of the events detected by W2B0 at T_e^c are not detected through v_x (f_{plr}). Figure 10 shows an example of a local change event detected solely by W2B0. Figures 10(a)–10(b) show that for v_x and f_{plr}, the signal does not exhibit any strong deviation from the stick behavior modeled by the DLMs, and consequently their NMEs are small. However, the W2B0 signal significantly deviates from the predicted oscillatory behavior, see Fig. 10(c). The fact that there is no visible change in the f_{plr} quantifying the global changes of the network implies that the detected change of the force network is local. For this particular local change, we find that there is a large spike in the broken force, f_{bc}, defined as the sum of all (normal) forces at the contacts that are broken between time t and the following output time, see Fig. 10(d). The spike in f_{bc} is the result of a single large broken contact (there are only two broken contacts and the broken force on the other one is very small). The spike in
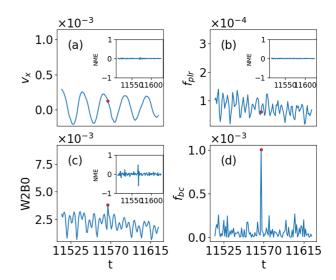

FIG. 10. Example of an event detected by the W2B0 at $T_e = 0.4$ that is not detected by v_x or f_{plr} at $T_e = 0.1$. (a)–(c): v_x, f_{plr}, and W2B0 with the inset displaying the corresponding NME; (d) the broken contact force, f_{bc}. The red point marks the detection made by the W2B0 at $T_e = 0.4$. The fact that v_x and f_{plr} do not detect this event suggests that it corresponds to a local change in the force network. The corresponding spike in f_{bc} is the result of a single broken contact with a large force value. There are two broken contacts but the broken force on the other one is very small.

W2B0 occurs at the same time, indicating that, at least for this local change event, the change in W2B0 is strongly related to broken contacts. We note that similar local changes, including nonaffine motion or rotations of the particles, have been discussed in previous works [15,21].

Now we turn our attention to the relation between the slip events detected by the off-line method and events detected by the DLMs. At each T_e, we match the events detected by the DLMs to the slip events. To better understand the composition of the matched events, we use two ratios: true positive rate and false positive rate. For a given DLM, the true positive rate, $r_{tp}(T_e)$, is the ratio of the number of slip events that are detected by the DLM, and the total number of slip events. The false positive rate, $r_{fp}(T_e)$, is the ratio of the events detected by the DLM that do not match any slip event, to the total number of events detected by the DLM. The large false positive rates are caused by the fact that the DLMs also detect microslip events and local change events, which are not detected by the off-line method. At this point, we cannot reliably predict which local change events will lead to a slip event. Further research will be necessary to address this issue.

Figure 11 depicts the ratios, $r_{tp}(T_e)$ and $r_{fp}(T_e)$. Figure 11(a) shows that for each DLM there is a range of values T_e for which $r_{tp}(T_e) = 1$ and thus each DLM is capable of detecting all slip events. For every DLM there is a considerable number of false positives at $T_e = T_e^c$, see Fig. 11(b). Initially, $r_{fp}(T_e)$ decreases for all the measures but then it increases for both v_x and f_{plr} (dashed lines). As before, this increase is caused by detecting the aftershocks as separate events, see Fig. 9. Thus, we also consider an adjusted $r_{fp}(T_e)$ in which the aftershocks are not included. Figure 11(b) shows
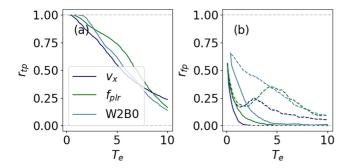
FIG. 11. (a) True positive rate, $r_{tp}(T_e)$, and (b) false positive rates, $r_{fp}(T_e)$. The dashed line marks the false positive rate and the solid line marks the adjusted false positive rate obtained by removing the aftershocks.

that the adjusted $r_{fp}(T_e)$ is always decreasing and drops much faster than the nonadjusted $r_{fp}(T_e)$.

To further justify our earlier classification of the events detected by v_x into slips and microslips we return to Fig. 9(b). The slope of the curve representing the adjusted number of events detected by v_x changes the fastest around the value of T_e (we call it the change point) where it crosses the dashed line representing the number of slip events detected by the off-line method. This is indicative of the presence of two classes of events [35,47]. Since at the change point the number of adjusted events is close to the number of slip events, and r_{fp} for v_x becomes zero (therefore the microslip events completely disappear), the two classes mentioned above directly correspond to slip and microslip events. That is, the distinction between the two types of events is not artificial, but reflective of an inherent difference between them.

The same argument that we used for v_x demonstrates that the events detected by f_{plr} also split into two classes roughly corresponding to slip and microslip events. This suggests that during slip and microslip events there is a close connection between the wall activity and the global rearrangements of the force network measured by f_{plr}. The W2B0 measure does not yield a separation of events into two obvious classes because the number of adjusted events detected by the DLM for W2B0, see Fig. 9(b), does not exhibit any clear change point. Thus, the connection between the wall activity and local changes of the force network, measured by W2B0, is much less obvious, since local changes may or may not lead to a slip or microslip event.

To further investigate the relation between wall movement and force network rearrangements, we introduce a different measure, $T_e^m > T_e$, which is defined as the largest value of T_e for which an event is still detectable. Figure 12 shows the relation between the values of T_e^m obtained by different measures, with each point corresponding to an event detected by both measures specified on the axes labels.

For both slip and microslip events, Fig. 12(a) demonstrates a linear relation between the magnitudes by which the horizontal wall velocity (v_x) and the global change of the force network (f_{plr}) deviate from the behavior expected in the stick regime. Note that the slope of the data points in this figure is different for the slip and microslip events. For the slip events, the wall speed increases more rapidly with f_{plr}. We note that
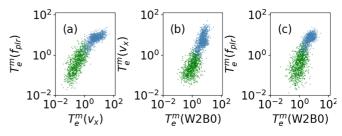

FIG. 12. Scatter plot of the T_e^m values for events detected at T_e^c by both considered measures (a) v_x and f_{plr}, (b) W2B0 and v_x, and (c) W2B0 and f_{plr}. The blue color indicates slip events while the green color indicates microslip events.

if T_e^m obtained by f_{plr} is larger than ≈ 3, then the event is almost certainly a slip event [see also Fig. 11(b)], while the events with $T_e^m < 1$ are microslips. Thus, there is a relatively well-defined critical value for the size of the global change of the force network, and surpassing this value leads to a slip event. Figure 12(b) indicates that determining whether a local change event will cause a slip event or not is more complicated. While very large (small) values of T_e^m always correspond to a slip (microslip) event, there is a wide range of the values T_e^m obtained by W2B0 for which we observe both slip and microslip events.

Next, we explore the relation between the value of T_e^m and the wall displacement during a detected event. Figure 13(a) shows that the values of T_e^m obtained by the v_x measure are linearly proportional to the wall displacement. We also observe a relatively clear distinction between microslip and slip events, since the data in Fig. 13(b) shows a clear change of slope around the boundary between the slip and microslip events. This change further indicates that for the slip events the wall activity increases more rapidly with the growing global change in the force network, than for the microslips. Figure 13(c) relates the size of the local change of the force network and the wall displacement. Similarly to Figs. 12(b)–12(c), there is a large range of values T_e^m obtained by W2B0 for which both slip and microslip events can occur. A local change of the force network with T_e^m in this range has uncertain consequences. It might dissipate without causing a global change in the force network or trigger a global change accompanied by a microslip or slip event. However, suffi-
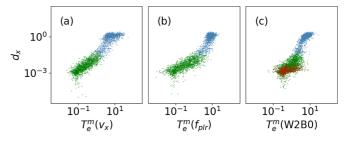

FIG. 13. Scatter plot of the wall displacement d_x during an event and its values T_e^m, for events detected at T_e^c by (a) v_x, (b) f_{plr}, and (c) W2B0. The blue color indicates slip events while the green color denotes microslip events. In c) the red color indicates local change events, as in Fig. 10. During a local change event, the wall movement [global change] is too small to be detected by v_x [f_{plr}].
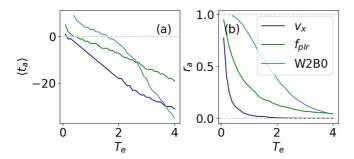
FIG. 14. Comparison of off-line and online methods: (a) the median advance notice $\langle t_a \rangle$ taken over slip events detected by the given measure at T_e; (b) the ratio of slip events detected in advance $r_a(T_e)$.

ciently small local changes never trigger a slip event while sufficiently large ones always do.

C. Predictive power of different measures

So far, we have compared the events detected by individual measures. It is also of interest to examine how early the slip events, identified by the off-line method, can be detected by DLMs. Figures 7(a)–7(c) suggest that the time at which the start of a slip event is detected by a DLM depends on both the considered measure and T_e. To examine this quantitatively, we consider the times at which the off-line method detects the start of the slip events as a baseline and compare them with the times obtained by different measures and values of T_e. We emphasize that the purpose of this comparison is quantifying the effectiveness of the online methods based on DLMs, and not comparing the performance of online and off-line methods. The off-line approach uses future data for identifying slip events and is not appropriate for predictive purposes.

For a given slip event, let t_0 and $t_0'(T_e)$ be the times at which it is detected by the off-line method, and by the DLM for the considered measure, respectively. We then define $t_a(T_e) = t_0 - t_0'(T_e)$. If $t_a(T_e) > 0$, then the slip event is identified in advance. To analyze how much in advance the slip events can be detected, using different measures and values of T_e, we consider the median advance notice $\langle t_a \rangle$ defined as follows. For a given measure and T_e, the value $\langle t_a \rangle(T_e)$ is the median over all slip events detected by the DLM. Figure 14(a) shows this metric as a function of $T_e \geqslant T_e^c$. We immediately observe that the $W2B0$ measure tends to provide the earliest detection times for a wide range of T_e's. In particular, for $T_e = T_e^c$, the median advanced notice is over ten time units, while the best value that can be achieved by f_{plr} is only around five, and v_x barely detects slip events in advance at all. We note that the amount of cross correlation is not particularly useful for predicting purposes, since the cross correlation is dominated by the long stick periods and is rather insensitive to the differences between the measures that appear around the onset of slip events.

To obtain the portion of the slip events that are detected in advance, we divide their number by the number of all slip events. This fraction is denoted by $r_a(T_e)$. Figure 14(b) shows that r_a, as expected, decreases with T_e for each considered measure. Once again, the shape of the W2B0 curve is different from the other two. This curve decreases slower and is the
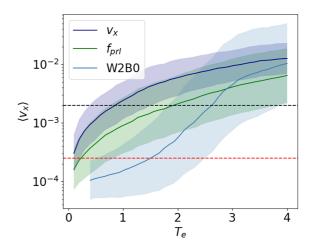

FIG. 15. Median magnitude of the wall velocity at the start of slip events detected at T_e by different measures. For each measure, the solid lines mark the median of v_x, and the shaded regions mark one standard deviation. The dashed lines show the two thresholds used by the off-line method: (black) v_l used to identify slip events and (red) v_s used to identify their start.

only one that approaches unity as T_e gets close to T_e^c. Hence the detection method based on this measure is the only one that can predict almost all slip events in advance for $T_e \leqslant 0.9$.

Finally, we investigate how fast the wall moves at the start of the slip event detected by different measures. Figure 15 shows the median of v_x at detection times as a function of T_e. The median at each fixed T_e value is taken over all slip events detectable by the given model and T_e. As expected, all the curves are increasing with T_e. Consistently with the results shown in Fig. 14, we find significantly lower values of $\langle v_x \rangle$ when considering the W2B0 measure. That is, the detection based on the W2B0 measure takes place before the wall has begun to move appreciably.

IV. CONCLUSIONS

In this work we present a method for detecting the onset of slip events that can be used on the fly for an incoming stream of data. The method is based on the fact that the behavior of the system during slip events is very different from the one during the stick regime. In particular, we consider three different measures describing the system: the wall velocity v_x, maximum percolation force of the differential force network, f_{plr}, and the Wasserstein distance between the persistence diagrams quantifying the force networks, W2B0. For each of these measures, we build a dynamical linear model (DLM) capable of accurately predicting its behavior during the stick regime. However, the predictions provided by DLMs become inaccurate when the measures start to exhibit more complex behavior as the system approaches a slip event. Hence, to detect the upcoming slip event we analyze the differences between the predicted and observed values of these measures.

Our analysis based on v_x shows a clear distinction between slip and microslip events. We find that global changes in the network measured by f_{plr} are essentially always associated with a slip or a microslip event that follows them. In particular,

the measure f_{plr} provides a slightly earlier prediction of the upcoming slip events than v_x. By using the W2B0 measure we identify local changes of the force network, which might or might not spread over the force network and become global. We observe that only the local changes that become global are followed by a slip or microslip event. While microslips were reported in the previous works considering similar systems, see, e.g., Refs. [19,35], and local changes (called local avalanches) were discussed recently as well [21], we are not aware of such events being used for predictive purposes. From the predictive perspective, we note that the W2B0 measure shows the best performance, in terms of sensitivity. On the other hand, the high sensitivity of this measure also leads to a significant percentage of false positives, in the form of local changes that do not lead to slip events.

In summary, we observe the following timeline of the changes leading to a slip event. Typical slip events start with a local change in the force network. The size of this local change can be quantified by the amount by which the observed values of W2B0 measure deviate from the predicted values. This deviation roughly corresponds to an increase in the W2B0 measure. If the size of the local change is sufficiently large, then it always becomes global and triggers a slip event. On the other hand, a sufficiently small local change does not trigger a slip event. There is, however, a large range of local change sizes for which the outcome is uncertain; the initial local disruption may either dissipate or trigger a global change resulting in a microslip or even slip event. While the chronology of a slip described above has been discussed in the literature already, our method allows for precise quantification of this timeline.

As noted above, a significant fraction of the local changes of the force network fall into an intermediary range and may or may not result in a slip or microslip event. It would be very much of interest to explore whether there are distinguishing characteristics of local changes that could be used to predict if the given change will lead to a slip event. In this work, we use W2B0 to identify local changes. This measure only compares the topological properties of the force network encoded by the persistence diagrams. Hence precise geometry of the force network is not considered. Further research will be necessary to establish if the geometry of the force and/or contact networks can be used to predict the outcome of local changes. Our results suggest that the use of stochastic state space models and in particular DLMs could be a productive path in this direction.

ACKNOWLEDGMENT

[1] L. de Arcangelis, C. Godano, J. R. Grasso, and E. Lippiello, Statistical physics approach to earthquake occurrence and forecasting, Phys. Rep. **628**, 1 (2016).

[2] M. L. Falk and J. S. Langer, Deformation and failure of amorphous, solidlike materials, Annu. Rev. Condens. Matter Phys. **2**, 353 (2011).

[3] E. G. Daub and J. M. Carlson, Friction, fracture, and earthquakes, Annu. Rev. Condens. Matter Phys. **1**, 397 (2010).

[4] H. Kawamura, T. Hatano, N. Kato, S. Biswas, and B. K. Chakrabarti, Statistical physics of fracture, friction, and earthquakes, Rev. Mod. Phys. **84**, 839 (2012).

[5] S. Luding, Y. Jiang, and M. Liu, Un-jamming due to energetic instability: Statics to dynamics, Granular Matter **23**, 80 (2021).

[6] M. M. Scuderi, C. Marone, E. Tinti, G. D. Stefano, and C. Collettini, Precursory changes in seismic velocity for the spectrum of earthquake failure modes, Nature Geosci. **9**, 695 (2016).

[7] S. Lherminier, R. Planet, V. L. d. Vehel, G. Simon, L. Vanel, K. J. Måløy, and O. Ramos, Continuously Sheared Granular Matter Reproduces in Detail Seismicity Laws, Phys. Rev. Lett. **122**, 218501 (2019).

[8] P. A. Johnson, B. Ferdowsi, B. M. Kaproth, M. Scuderi, M. Griffa, J. Carmeliet, R. A. Guyer, P.-Y. Le Bas, D. T. Trugman, and C. Marone, Acoustic emission and microslip precursors to stick-slip failure in sheared granular material, Geophys. Res. Lett. **40**, 5627 (2013).

[9] B. Rouet-Leduc, C. Hulbert, N. Lubbers, K. Barros, C. J. Humphreys, and P. A. Johnson, Machine learning predicts laboratory earthquakes, Geophys. Res. Lett. **44**, 9276 (2017).

[10] N. Nerone, M. A. Aguirre, A. Calvo, D. Bideau, and I. Ippolito, Instabilities in slowly driven granular packing, Phys. Rev. E **67**, 011302 (2003).

[11] M. A. Aguirre, A. Calvo, I. Ippolito, A. Medus, and M. Mancuso, Rearrangements in a two-dimensional packing of disks, Phys. Rev. E **73**, 041307 (2006).

[12] T. Scheller, C. Huss, G. Lumay, N. Vandewalle, and S. Dorbolo, Precursors to avalanches in a granular monolayer, Phys. Rev. E **74**, 031311 (2006).

[13] V. Yu. Zaitsev, P. Richard, R. Delannay, V. Tournat, and V. E. Gusev, Pre-avalanche structural rearrangements in the bulk of granular medium: Experimental evidence, Europhys. Lett. **83**, 64003 (2008).

[14] L. Staron, J.-P. Vilotte, and F. Radjai, Preavalanche Instabilities in a Granular Pile, Phys. Rev. Lett. **89**, 204302 (2002).

[15] C. Maloney and A. Lemaitre, Subextensive Scaling in the Athermal, Quasistatic Limit of Amorphous Matter in Plastic Shear Flow, Phys. Rev. Lett. **93**, 016001 (2004).

[16] M. Pica Ciamarra, E. Lippiello, C. Godano, and L. de Arcangelis, Unjamming Dynamics: The Micromechanics of a Seismic Fault Model, Phys. Rev. Lett. **104**, 238001 (2010).

[17] P. Welker and S. McNamara, Precursors of failure and weakening in a biaxial test, Granular Matter **13**, 93 (2011).

[18] D. Denisov, K. Lorincz, J. Uhl, K. A. Dahmen, and P. Schall, Universality of slip avalanches in flowing granular matter, Nature Commun. **7**, 10641 (2016).

[19] J. T. Uhl, S. Pathak, D. Schorlemmer, X. Liu, R. Swinderman, B. A. W. Brinkman, M. LeBlanc, G. Tsenkenis, N. Friedman, R. Behringer, D. Denisov, P. Schall, X. Gu, W. J. Wright, T. Hufnagel, A. Jennins, J. Green, P. K. Liaw, T. Becker, G. Dresen

et al., Universal quake statistics: From compressed nanocrystals to earthquakes, Nature Sci. Rep. **5**, 16493 (2015).

[20] D. V. Denisov, K. A. Lőrincz, W. J. Wright, T. C. Hufnagel, A. Nawano, X. Gu, J. T. Uhl, K. A. Dahmen, and P. Schall, Universal slip dynamics in metallic glasses and granular matter–linking frictional weakening with inertial effects, Sci. Rep. **7**, 43376 (2017).

[21] J. Barés, D. Wang, D. Wang, T. Bertrand, C. S. O'Hern, and R. P. Behringer, Local and global avalanches in a two-dimensional sheared granular medium, Phys. Rev. E **96**, 052902 (2017).

[22] M. Kramar, R. Basak, C. Cheng, and L. Kondic, On intermittency in sheared granular systems, Soft Matter **18**, 3583 (2022).

[23] G. Petris, S. Petrone, and P. Campagnoli, *Dynamic Linear Models with R* (Springer, New York, 2009).

[24] G. Evensen, *Data Assimilation: The Ensemble Kalman Filter* (Springer, New York, 2009).

[25] Y. Kwon and Y. Park, Improvement of vision guided robotic accuracy using kalman filter, Comput. Ind. Eng. **65**, 148 (2013).

[26] L. D. Stone, R. L. Streit, T. L. Corwin, and K. L. Bell, *Bayesian Multiple Target Tracking* (Artech House, Norwood, 2014).

[27] L. Zhao, X. Feng, and C. H. Meyer, Direct and accelerated parameter mapping using the unscented kalman filter, Magn. Reson. Med. **75**, 1989 (2015).

[28] R. Shankar, K. Chatterjee, and T. K. Chatterjee, A very short-term load forecasting using kalman filter for load frequency control with economic load dispatch, J. Eng. Sci. Technol. **5**, 97 (2012).

[29] H. Wang, Q. Qian, and A. Tordesillas, Modeling big spatio-temporal geo-hazards data for forecasting by error-correction cointegration and dimension-reduction, Spat. Stat. **36**, 100432 (2020).

[30] S. Das and A. Tordesillas, Near real-time characterization of spatio-temporal precursory evolution of a rockslide from radar data: Integrating statistical and machine learning with dynamics of granular failure, Remote Sens. **11**, 2777 (2019).

[31] F. Dalton and D. Corcoran, Self-organized criticality in a sheared granular stick-slip system, Phys. Rev. E **63**, 061312 (2001).

[32] P. A. Johnson and X. Jia, Nonlinear dynamics, granular media and dynamic earthquake triggering, Nature (London) **437**, 871 (2005).

[33] P. A. Johnson, H. Savage, M. Knuth, J. Gomberg, and C. Marone, Effects of acoustic waves on stick–slip in granular media and implications for earthquakes, Nature (London) **451**, 57 (2008).

[34] A. A. Long, D. V. Denisov, P. Schall, T. C. Hufnagel, X. Gu, W. J. Wright, and K. A. Dahmen, From critical behavior to catastrophic runaways: Comparing sheared granular materials with bulk metallic glasses, Granular Matter **21**, 99 (2019).

[35] L. de Arcangelis, M. P. Ciamarra, E. Lippiello, and C. Godano, Micromechanics and statistics of slipping events in a granular seismic fault model, J. Phys.: Conf. Ser. **319**, 012001 (2011).

[36] O. Dauchot, G. Marty, and G. Biroli, Dynamical Heterogeneity Close to the Jamming Transition in a Sheared Granular Material, Phys. Rev. Lett. **95**, 265701 (2005).

[37] E. Stanifer and M. L. Manning, Avalanche dynamics in sheared athermal particle packings occurs via localized bursts predicted by unstable linear response, Soft Matter **18**, 2394 (2022).

[38] L. Kovalcinova, A. Goullet, and L. Kondic, Scaling properties of force networks for compressed particulate systems, Phys. Rev. E **93**, 042903 (2016).

[39] J. A. Dijksman, L. Kovalcinova, J. Ren, R. P. Behringer, M. Kramár, K. Mischaikow, and L. Kondic, Characterizing granular networks using topological metrics, Phys. Rev. E **97**, 042903 (2018).

[40] P. A. Cundall and O. D. L. Strack, A discrete numerical model for granular assemblies, Géotechnique **29**, 47 (1979).

[41] A. Zomorodian and G. Carlsson, *Computing Persistent Homology* (Springer, Berlin, 2004).

[42] M. Kramár, A. Goullet, L. Kondic, and K. Mischaikow, Quantifying force networks in particulate systems, Physica D **283**, 37 (2014).

[43] M. Kramár, A. Goullet, L. Kondic, and K. Mischaikow, Persistence of force networks in compressed granular matter, Phys. Rev. E **87**, 042207 (2013).

[44] M. Kramár, A. Goullet, L. Kondic, and K. Mischaikow, Evolution of force networks in dense particulate media, Phys. Rev. E **90**, 052203 (2014).

[45] G. M. Ljung and G. E. P. Box, On a measure of lack of fit in time series models, Biometrika **65**, 297 (1978).

[46] S. S. Shapiro and M. Wilk, An analysis of variance test for normality (complete samples), Biometrika **52**, 591 (1965).

[47] T. Mori and H. Kawamura, Simulation study of the one-dimensional burridge-knopoff model of earthquakes, J. Geophys. Res. Solid Earth **111**, B07302 (2006).